

Imaging acoustic waves by microwave microscopy

Lu Zheng¹, Linbo Shao², Marko Loncar², Keji Lai^{1*}

¹Department of Physics, University of Texas at Austin

²John A. Paulson School of Engineering and Applied Sciences, Harvard University

*kejilai@physics.utexas.edu

Atoms in all materials are constantly shaking, which is largely responsible for the transfer of heat and sound. In a uniform crystalline solid, the motion of the lattice can be decomposed into just a handful of normal modes of vibration, or in the language of quantum mechanics, a set of quantized eigenmodes of the elastic structure known as phonons [1]. In the frequency (f) regime of interest for microwave engineers, there exist three (one longitudinal, two shear) branches of vibrational modes with long wavelengths – ‘long’ when compared with the atomic spacing. Their frequencies, which represent the energy of each quantum, are linearly proportional to the inverse wavelengths, which represent the momentum of each quantum. The ratio between the two is typically several kilometers per second. In good crystals with few imperfections, these vibrations travel very long distance – ‘long’ when compared with the wavelength – with little decay of the amplitude under the ambient temperature and pressure. At audio frequencies, these sound waves can propagate in solids. They are commonly known as acoustic waves.

The connection between acoustic waves and microwave electronics dated back to the 1950s, when scientists in the Bell Labs demonstrated the generation and detection of few-GHz longitudinal and shear waves in quartz crystals [2]. It was soon recognized that, because the speed of sound in solids is 10^5 times smaller than the speed of light, microwave acoustic devices using piezoelectric transducers [3] could afford substantial miniaturization in the system dimension. In particular, compact resonators that take advantage of the ultralow loss of bulk acoustic waves (BAWs) in quartz have found widespread application in professional electronic equipment [4]. Starting from the late 1960s, much attention was directed to the guided waves along the free surface of materials [5], which were first explained by Lord Rayleigh in his seminal 1885 paper [6]. Named after the discoverer, Rayleigh waves or surface acoustic waves (SAWs) have lower speed than BAWs and low propagation loss. They are easily accessible from the surface and readily compatible with the planar technology developed for integrated semiconductor devices. To date, SAW devices such as delay lines, filters, oscillators, transformers, and sensors are indispensable

in most microwave systems [7, 8] and will continue to thrive in the 5G era. It is anticipated that the global SAW market will reach a remarkable number of \$3.4B by the end of 2024 [9].

The characteristic dimension of SAW devices using interdigital transducers (IDTs) is set by the acoustic wavelength in piezoelectric solids, which is typically a few micrometers at 1 GHz. In other words, the inherent length scale to observe wave phenomena, such as interference, diffraction, and localization of SAWs, is in the mesoscopic regime. High-resolution imaging of the acoustic displacement field or the accompanying electric field is therefore highly desirable for designing, characterizing, and ultimately improving the SAW devices [7]. Moreover, it has been shown that, in artificial structures with periodic piezoelectric properties, the coupling between GHz electromagnetic waves (photons) and acoustic waves (phonons) can lead to polaritons with different phononic bands [10-15]. Spatial mapping of the SAW fields, in conjunction with numerical simulations of the phononic metamaterials, is thus of great interest to advance this research field.

In the past few decades, microscopy techniques have evolved rapidly to provide various means to visualize GHz acoustic waves. Fig. 1a shows an image of surface waves taken by stroboscopic x-ray topography [18]. Here the ‘strobe’ is obtained by phase lock between the x-ray source and the excitation of the SAW device, resulting in a stationary image of the propagating surface wave [16 – 18]. A major drawback of the technique is the need of coherent X-rays from a synchrotron radiation light source, which limits its widespread use in the laboratory scale. A somewhat related technique that also utilizes light to visualize acoustic displacement is the scanning laser reflectometry [19, 20] or interferometry [21 – 23]. The technique can resolve sub-picometer out-of-plane displacement with sub-nanosecond temporal resolution, as exemplified by the beautiful snapshot of the propagating wave on (001) TeO_2 surface [21] in Fig. 1b. The lateral spatial resolution, however, is diffraction-limited to $\sim 1 \mu\text{m}$ due to the use of visible laser. In the early 1990s, it was also demonstrated that the secondary electrons in a scanning electron microscope (SEM) could be modulated by the SAW electric field, forming a stationary pattern of the propagating wave [24 – 26] (Fig. 1c). The applicability of this method, however, is rather limited due to the strong charging effect in insulating piezoelectric crystals, resulting in a moderate resolution of about $1 \mu\text{m}$ and an operation frequency below 0.5 GHz.

The advent of scanning probe microscopy has brought in new impetus to image SAWs with nanoscale spatial resolution. In a typical atomic-force microscopy (AFM) setup, the mechanical resonance of the cantilever of several hundred kHz is far below the microwave regime. As a result, the scanning acoustic force microscopy (SAFM) works in a heterodyne scheme [27 - 31], which mixes the acoustic sample wave with a slightly detuned reference wave from another source. This leads to cantilever oscillations at a difference frequency being measured by the conventional photodiode detection (Fig. 1d). Similarly, by mixing a signal at the mechanical resonance of the probe and a second component at the microwave frequency, the dynamic electrostatic force microscopy (EFM) can measure the cantilever deflection due to the piezoelectric polarization field. Fig. 1e shows such an EFM image of the interference pattern arising from a metal reflector on a SAW device [32]. Finally, the surface oscillation excited by propagating SAWs can be imaged by stroboscopic scanning tunneling microscopy (STM) [33 – 36], as shown in Fig. 1f. The interested readers are referred to the review article by Hesjedal [31] for a comprehensive coverage of these techniques.

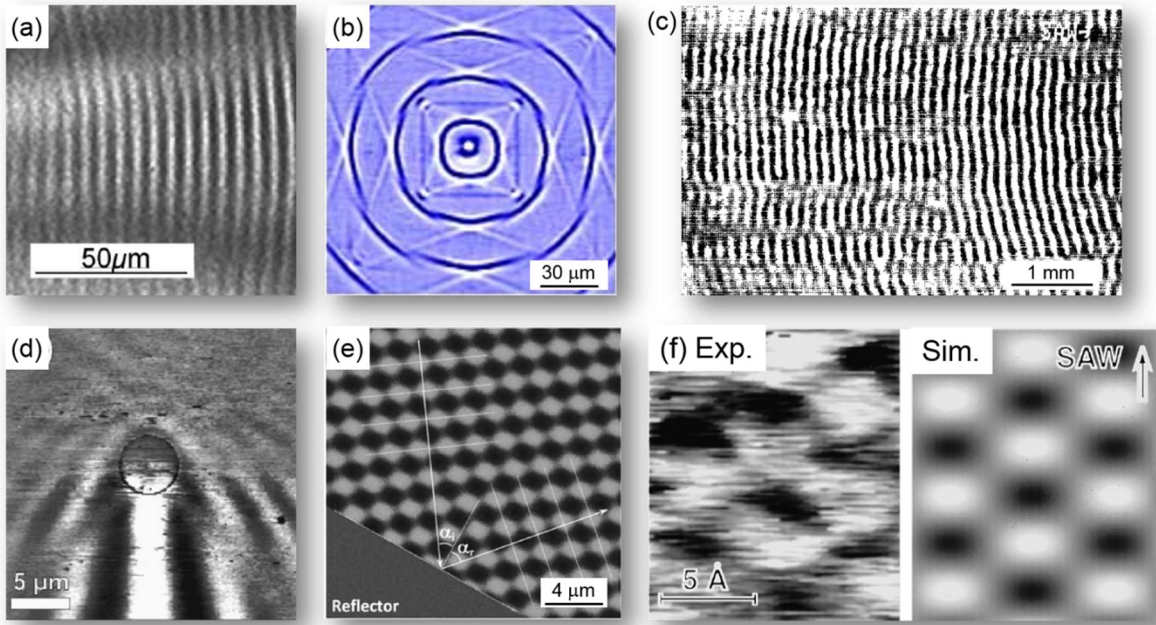


Figure 1. (a) Stroboscopic X-ray topograph of travelling Rayleigh waves on GaAs taken with the driving signal phase locked to the synchrotron radiation emission [18]. The SAW is excited at 579 MHz. (*Printed with the permission of American Institute of Physics from W. Sauer et. al. Appl. Phys. Lett. 75, 1709 (1999) [18].*) (b) Surface phonon image on the (001) TeO_2 surface taken by pump-probe scanning laser interferometry [21]. SAWs are thermoelastically excited by the 415 nm pump laser with a repetition rate of 80 MHz. (*Printed with the permission of American Physical Society from Y. Sugawara et. al. Phys. Rev. Lett. 88, 185504 (2002) [21].*) (c) Scanning electron photographs of the

traveling SAW on LiNbO₃ [24]. The excitation frequency is 25.127 MHz. (*Printed with the permission of American Institute of Physics from D. V. Roshchupkin et. al. Appl. Phys. Lett. 60, 2330 (1992). [24]*) (d) SAFM amplitude image on (001) GaAs [27]. A scattering dot (Au, diameter 5 μm) is denoted by the black circle in the center. The SAW is excited at 694 MHz and a nearby IDT (not shown) sends a slightly detuned signal for the SAFM imaging. (*Printed with the permission of American Institute of Physics from T. Hesjedal et. al. Appl. Phys. Lett. 78, 1948 (2001). [27]*) (e) Dynamic EFM image of SAW interference near a metal reflector, showing both the incident and reflected wave fronts. The tip resonant frequency is ~ 75 kHz and the SAW is excited at 1.585 GHz [32]. (f) Comparison between measured (left) and modeled (right) STM images of Au (111) surface excited at 39.5 MHz and clocked at 39.51 MHz [36]. (*Printed with the permission of American Institute of Physics from T. Hesjedal et. al. Appl. Phys. Lett. 69, 354 (1996). [36]*)

Despite some success of SAFM/EFM/STM to image the SAW displacement field, the spatial distribution of SAW electric field, which is of paramount importance for electronic applications, has not been thoroughly studied. In an early attempt to map out the piezoelectric surface potential (Fig. 2a), a tungsten tip at the end of a coaxial cable raster scanned on LiNbO₃ and the detected SAW signal was demodulated by microwave analyzer [37]. While this simple configuration did capture the basic idea, it is clear that much more engineering effort is needed to perform nanoscale SAW imaging. The modern version of the probe (Fig. 2b) is wafer-scale micro-fabricated cantilever tips with electrical shielding and sub-100nm tip apex [38]. These probes are commercially available from PrimeNano Inc. Fig. 2c shows a close-up view of the experimental apparatus, where microwave signals are fed to both the tip and the SAW device. The atomic-force microscopy (AFM) platform provides the necessary topographic feedback for high-resolution imaging work.

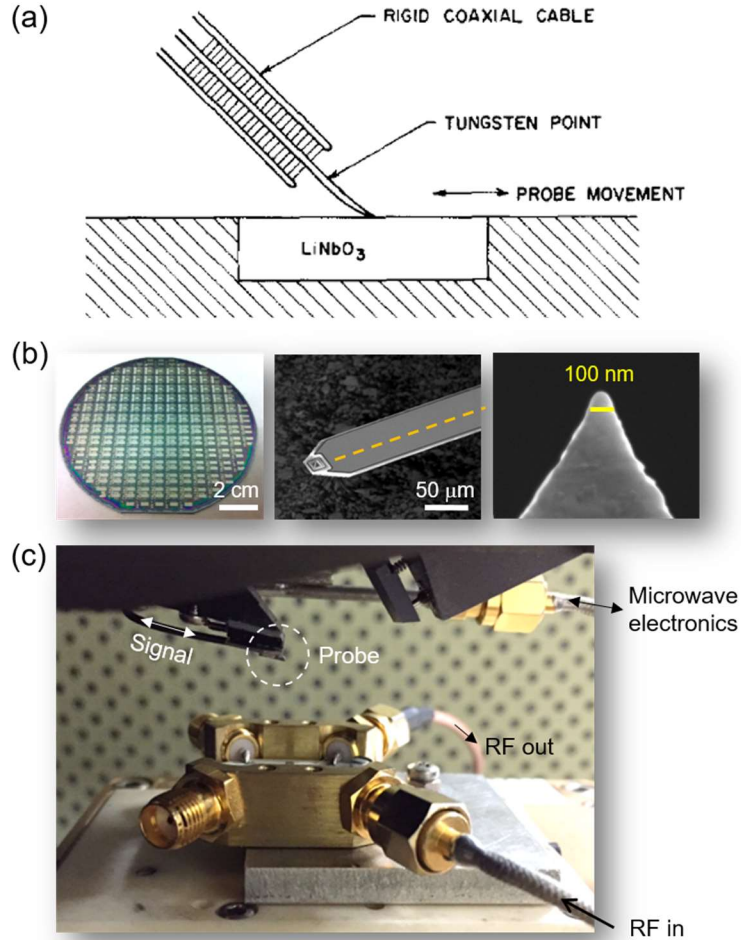


Figure 2. (a) Experimental setup of an early attempt to probe the SAW electric field [37]. (*Printed with the permission of American Institute of Physics from B. A. Richardson et. al. Appl. Phys. Lett. 16, 82 (1970). [37]*) (b) From left to right: Batch-fabricated probes on a 4-inch wafer; cantilever with metallic shield and buried center conductor (orange dashed line); close-up view of the tip apex [38] (*Printed with the permission of IOP Publishing from Y. Yang et. al. J. Micromech. Microeng. 22, 115040 (2012) [38]*). (c) Picture of the AFM-based setup for imaging SAW devices with RF connections. (*Photographed by Keji Lai. Used with permission.*)

Microwave Impedance Microscopy

The schematic of a typical microwave microscope is depicted in Fig. 3a. In this mode of operation, the microwave signal is delivered to the center conductor of the tip through an impedance-match (Z-match) section. The reflected signal is amplified and demodulated by an in-phase quadrature (IQ) mixer. As seen from the equivalent circuit in Fig. 3b, the microwave electronics is detecting the small variation of tip-sample impedance Z_{t-s} during the raster scan, thus the term of microwave impedance microscopy (MIM) [39,40]. By adjusting the local oscillator (LO) phase ϕ , the real and imaginary components of the admittance change $\Delta Y_{t-s} = (Z_{t-s})^{-1}$ can be

mapped as MIM-Re and MIM-Im images, respectively. It should be noted that most microwave microscopy works in the literature, although with different acronyms, are based on the same underlying physics. The reflection-mode MIM (RMIM) is widely used to study the nanoscale permittivity and conductivity distribution in advanced materials, which is surveyed by other articles in this special issue. We will show later that the technique can also offer insights to the piezoelectric transduction in ferroelectric materials.

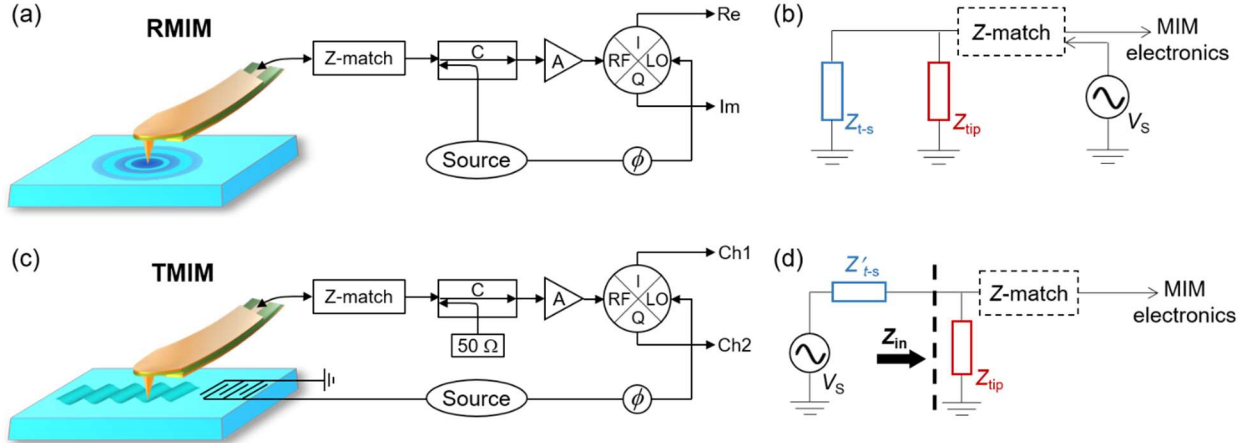


Figure. 3 (a) Schematic of the RMIM [39,40]. The excitation signal is delivered to the tip and the reflected signal is amplified and demodulated by the IQ mixer to form the RMIM-Re and RMIM-Im images. C: coupler, A: amplifier, ϕ : phase shifter. (b) Equivalent circuit of the RMIM. (c) Schematic of the TMIM [41]. The excitation signal is delivered to the IDT on the sample, and the transmitted signal is amplified and demodulated by the IQ mixer to form the TMIM-Ch1 and TMIM-Ch2 images. (d) Equivalent circuit of the TMIM. (Printed with the permission of American Physical Society from L. Zheng et. al. *Phys. Rev. Appl.* 9, 061002 (2018). [41])

The RMIM can be easily reconfigured in the transmission-mode (TMIM) to perform direct imaging of SAW electric fields [41]. As illustrated in Fig. 3c, the microwave signal is delivered to the IDT on a piezoelectric sample and the tip acts as a movable receiver. The oscillating SAW field coupled to the tip is then demodulated as two orthogonal output channels TMIM-Ch1 and -Ch2. The equivalent circuit of the TMIM configuration is shown in Fig. 3d. The time-varying source potential V_s is picked up by the tip, followed by the same amplification and demodulation in the microwave electronics. Specifically, the input signal to the TMIM tip is given by

$$V_{in} = V_s \cdot Z_{in} / (Z'_{t-s} + Z_{in}) \approx V_s \cdot Z_{in} / Z'_{t-s} \quad (1)$$

, where $|Z_{in}| \sim 1 \text{ K}\Omega$ is the effective input impedance of the tip / Z-match section as the receiver and $|Z'_{t-s}| \sim 100 \text{ K}\Omega$ is the tip-sample coupling impedance [41]. It should be noted that similar transmission-type probes have been used to map out the RF fields in microwave resonators [42],

43] and metamaterials [44, 45]. In those systems, however, the characteristic length scale is set by the electromagnetic rather than acoustic wavelength and the mesoscopic resolution is not necessary.

Before discussing the experimental results, we would like to point out that in conventional microwave microscopy where the electrical property is of interest, RMIM and TMIM will provide similar information on the local variation of permittivity or conductivity. In the presence of a piezoelectric transducer that launches a propagating SAW, however, the two may yield rather different information of the sample, which will be elaborated below.

RMIM Results

Most microwave imaging of SAWs to date has been carried out on LiNbO_3 , an important acousto-electronic and acousto-optic material for its high piezoelectric constant [46], low acoustic attenuation [47, 48], and strong nonlinear optical coefficients [49, 50]. LiNbO_3 has a trigonal (class 3m) crystal structure with a mirror yz plane and a direct triad z -axis along the polar direction [46]. It is a ferroelectric material and the spontaneous polarization can be switched by electrical poling [49]. Fig. 4a shows the simplest scenario around a lithographically defined straight domain wall (DW) on a z -cut LiNbO_3 sample [51]. The two oppositely polarized domains are seen in the piezo-force microscopy (PFM) image in Fig. 4b. The RMIM-Re image taken at $f = 967$ MHz, on the other hand, exhibits clear interference fringes around the DW. Because the electrical conductance of the insulating LiNbO_3 is negligible, the RMIM-Re contrast clearly indicates that the microwave energy is dissipated through the piezoelectric transduction rather than the Ohmic loss.

The main features of the microwave image include a prominent dip at the DW and damped oscillations with a periodicity of 4.5 μm away from the wall. It is certainly tempting to interpret these fringes as the standing-wave pattern of the acoustic displacement field underneath the tip [52]. However, should it be the case, the measured periodicity would indicate the dominance of a guided wave with an unphysically large phase velocity of 8.8 km/s. In fact, since the acoustic impedance is the same for both domains, the reflection of displacement fields from the yz DW should be rather weak for acoustic waves. The RMIM-Re interference pattern in Fig. 4b is therefore nontrivial and calls for a careful analysis of the tip-sample interaction.

As shown in Fig. 4c, the measured $1/\lambda$ (λ being the period of the RMIM-Re fringes) scales with the microwave frequency from 285 MHz to 6 GHz. The slope of 4.4 ± 0.2 km/s closely

matches that of the pseudo-SAW (P-SAW) [53, 54], which only exists on the surface of piezoelectric materials. The dispersion of this surface wave lies in the continuum of bulk waves and its energy leaks into the bulk during the propagation [54]. Unlike the Rayleigh SAW, the displacement field of this Bleustein–Gulyaev-like SAW [55, 56] is primarily polarized in the y -direction [57], although the wave is not purely transverse-horizontal due to the lack of an even-order symmetry axis in LiNbO_3 .

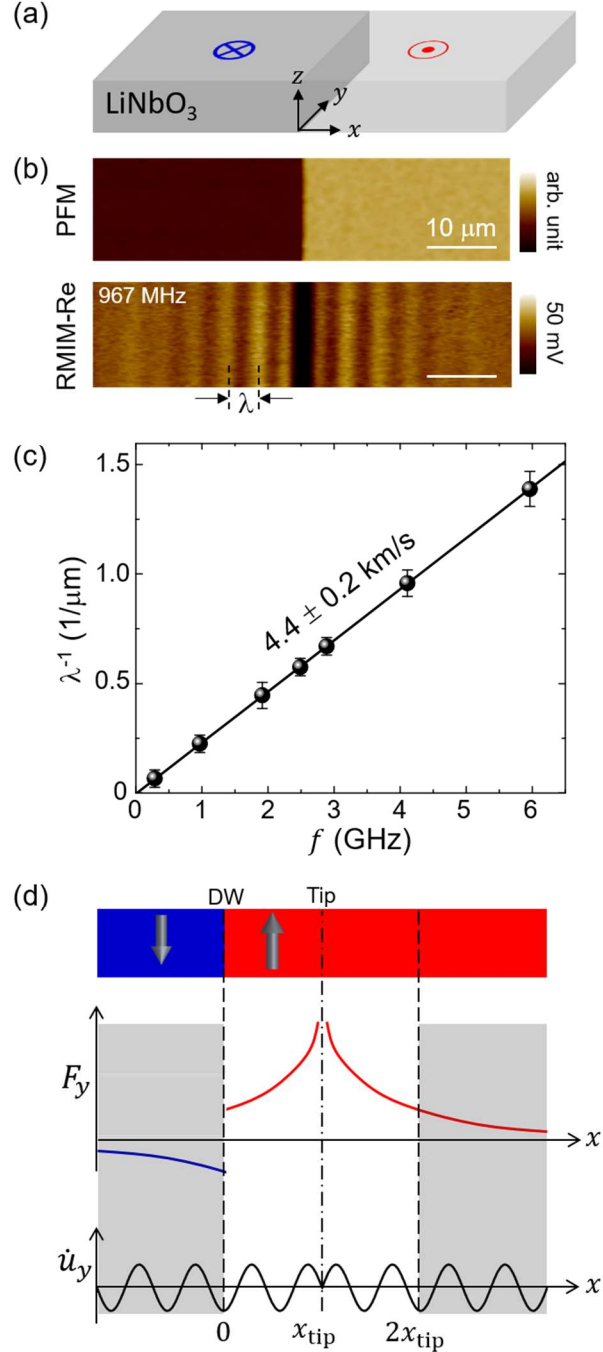


Figure 4. (a) Schematic of the z -cut LiNbO_3 sample with a single domain wall. (b) PFM phase (top) and RMIM-Re (bottom) images of the sample [51]. Spacing of the bright fringes is labeled as λ . Scale bars are $10 \mu\text{m}$. (c) Linear relation between λ^{-1} and the RMIM frequency. The slope corresponds to a wave velocity of $4.4 \pm 0.2 \text{ km/s}$. (d) *Top*: Schematic view of the tip–sample configuration in the xz -plane. *Middle*: Sketch of the y -component of the electromechanical force. *Bottom*: Time derivative of the displacement field near the surface. The sign of F_y is flipped in opposite domains. The overlap integral of $F_y \cdot \dot{u}_y$ in the two shaded areas cancels each other [51]. (*Printed with the permission of United States National Academy of Sciences from L. Zheng et. al. Proc. Natl. Acad. Sci. 115, 5338 (2018) [51]*).

Given the background information, the RMIM result can be understood as follows. In LiNbO_3 , the local mechanical strain and electric field are coupled by the 3rd-rank piezoelectric tensors, whose signs are flipped across opposite domains [46]. The RMIM-Re measures the loss in electrical power, which by energy conservation equals the gain in mechanical power of various acoustic waves in solids. Since the P-SAW is dominated by the y -component of its displacement fields [57], the power transduction is predominantly determined by the overlap between F_y and \dot{u}_y , the y -components of the electromechanical force density and time derivative of the displacement, respectively. As seen in Fig. 4d, F_y flips sign in different domains, whereas \dot{u}_y is an even function with respect to the tip position. The overlap integral in the two shaded areas cancels each other, leading to a drop in power transduction when the tip is close to the wall. As the tip moves away from the DW, the truncated overlap integral oscillates with one-wavelength periodicity and shows the damping in amplitude. Note that the analysis here only provides a qualitative physical picture. For a more in-depth discussion, the readers are referred to Ref. [51] for the full numerical simulation of the acoustic fields and power transduction.

The interference of piezoelectric transduction can be further appreciated in LiNbO_3 coral domains formed by electrical poling [51]. Fig. 5a and 5b show the PFM and RMIM-Re images of four closed domains shaped in an equilateral triangle, a hexagon, a circle, and a square, respectively. Because of the crystal symmetry, straight DWs on the z -cut LiNbO_3 surface can only form along the three y -equivalent axes. Consequently, the domain designed to be a circle appears as a rounded hexagon and the domain designed to be a square appears as a distorted rectangle. Beautiful interference patterns due to the superposition of ripples around each DW are observed in the microwave images. At first sight, these visually attractive features (artistic rendering in Fig. 5c) are reminiscent of the electron waves in quantum corals imaged by STM [58]. In stark contrast to those standing-wave patterns, however, the adjacent nodes in the RMIM data are not spaced by half wavelength. The existence of such patterns does not indicate the presence of acoustic

resonance. In other words, the bright and dark regions in the RMIM-Re images mark the tip locations around which the piezoelectric transduction is highly effective and ineffective, respectively.

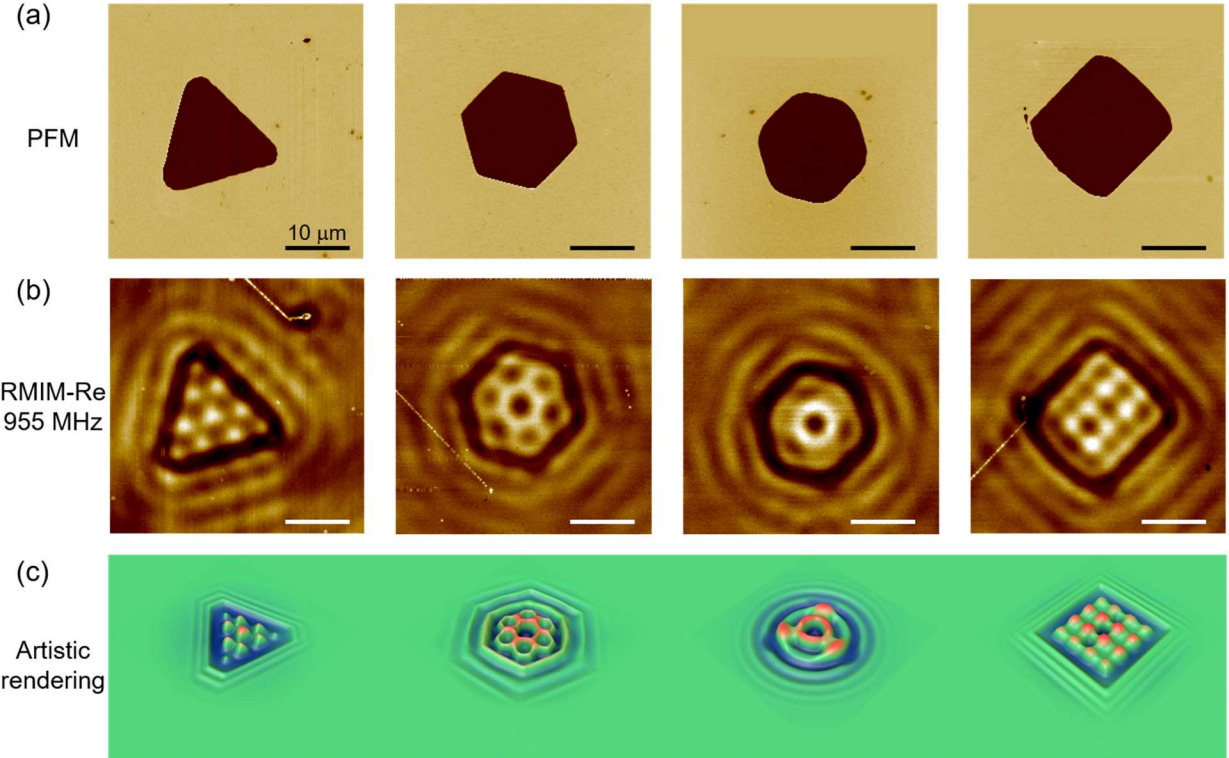


Figure 5. (a) PFM and (b) RMIM-Re images at $f = 955$ MHz of four closed LiNbO_3 domains. Interference patterns due to the superposition of ripples around each DW are seen in the microwave data [51]. Scale bars are $10 \mu\text{m}$. (c) Artistic rendering of the corresponding microwave images. (Printed with the permission of United States National Academy of Sciences from L. Zheng et. al. Proc. Natl. Acad. Sci. 115, 5338 (2018) [51]).

Putting these findings in perspective, the RMIM experiment reveals some internal degrees of freedom in piezoelectric and elastic tensors, which are not accessible by measurements of the acoustic displacement fields. On the other hand, the microwave electric field from the tip can excite many modes of acoustic waves in piezoelectrics, which may complicate the image analysis. For the purpose of SAW imaging, the TMIM detection of waves generated by external sources would be preferable, which will be reviewed in the next section.

TMIM Results

Fig. 6a shows the SEM image of an IDT designed to excite the x -propagating Rayleigh-type SAW on a z -cut LiNbO_3 crystal, which was poled to be a single ferroelectric domain prior to

the device fabrication. Figs. 6b and 6c display the simultaneously acquired AFM and TMIM images when the IDT was powered by a 10-dBm microwave at $f = 957$ MHz [41]. While only the interdigital fingers are seen in the surface topography, the electrical potential with a spatial periodicity consistent with the Rayleigh SAW ($v = 3.8$ km/s) [48] can be clearly imaged by TMIM. Here the tip picks up an input signal that is proportional to the SAW potential. Signals at the RF and LO ports of the mixer can be represented as $V_{\text{RF}} \propto V_s \propto e^{i(\omega t - kx)}$ and $V_{\text{LO}} \propto e^{i(\omega t + \phi)}$ (ω : angular frequency, k : acoustic wave vector, ϕ : mixer phase), respectively. Ignoring the terms containing $2\omega t$, one can see that the system demodulates the time-varying SAW potential into time-independent spatial patterns, which is observed in the TMIM data.

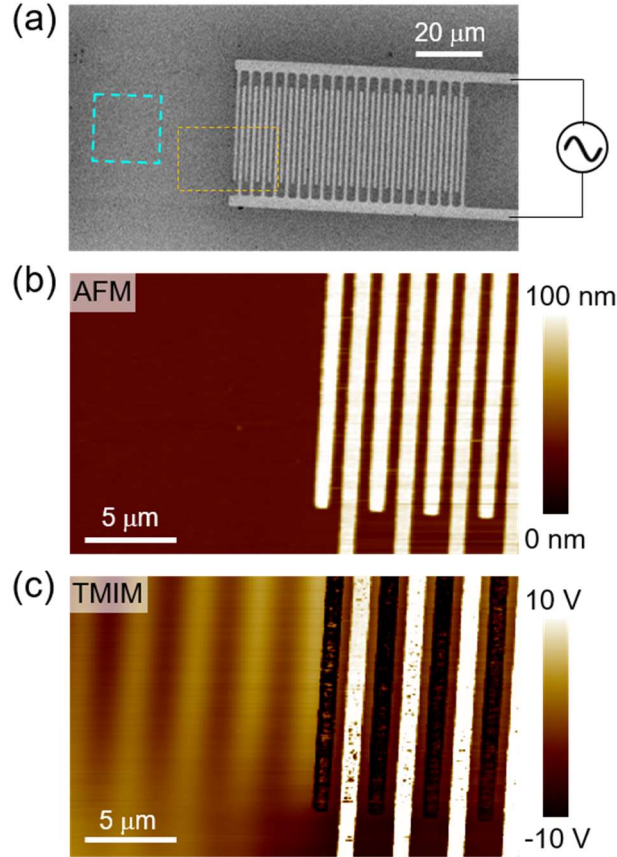


Figure 6. (a) SEM image of the SAW device. (b) AFM and (c) TMIM images in the dashed orange rectangle in (a). Wavelike features are seen in the TMIM data [41]. (*Printed with the permission of American Physical Society from L. Zheng et. al. Phys. Rev. Appl. 9, 061002 (2018). [41]*)

We now turn to the T-MIM imaging of a standing wave formed by two counter-propagating SAWs. Fig. 7a shows the schematic of the experimental setup, where two balanced signals (0 dBm in amplitude) with a phase offset of θ are fed into a pair of IDTs. This geometry is technologically

important in that it can create acoustic trapping potentials for electrons. Following the same analysis above, the input signals to the mixer can be written as $V_{\text{RF}} \propto e^{i(\omega t-kx)} + e^{i(\omega t+kx)}$ and $V_{\text{LO}} \propto e^{i\omega t}$. The LO phase ϕ is omitted since it contributes the same phase to both channels. The mixer then generates two output signals as follows.

$$V_{\text{Ch1}} \propto \text{Re}(V_{\text{RF}}V_{\text{LO}}^*) = \cos kx + \cos(kx + \theta) \quad (2)$$

$$V_{\text{Ch2}} \propto \text{Im}(V_{\text{RF}}V_{\text{LO}}^*) = -\sin kx + \sin(kx + \theta) \quad (3)$$

By tuning the phase difference θ between the two counter-propagating SAWs, the signal levels of the two TMIM channels can be varied. When $\theta = 0^\circ$, the sinusoidal spatial patterns are expected to appear only in Ch1 ($V_{\text{Ch1}} \propto 2 \cos kx, V_{\text{Ch2}} \propto 0$). The patterns should then be the same in both channels when $\theta = 90^\circ$ ($V_{\text{Ch1}} = V_{\text{Ch2}} \propto \cos kx - \sin kx$) and completely move to Ch2 when $\theta = 180^\circ$ ($V_{\text{Ch1}} \propto 0, V_{\text{Ch2}} \propto -2 \sin kx$). As seen in Fig. 7b, the predicted evolution is again in excellent agreement with the measured TMIM data. The results demonstrate that TMIM can image the interference of acoustic waves in piezoelectric materials.

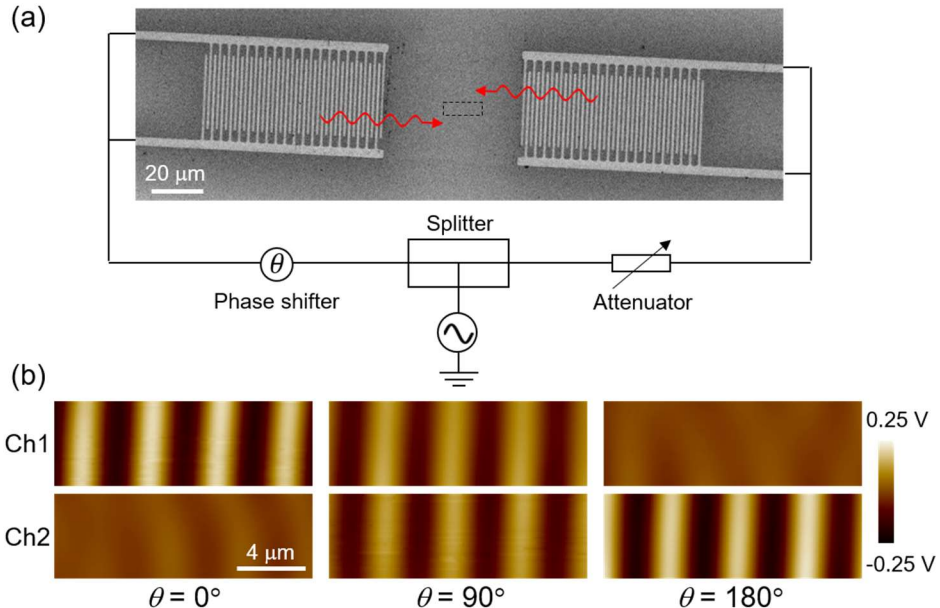


Figure 7. (a) Schematic diagram for the imaging of counter propagating waves. Two signals (0 dBm in amplitude and phase offset by θ) split from the same source are fed into the two IDTs. (b) TMIM images at different values of θ showing the transition of signal strength from Ch1 to Ch2 [41]. (Printed with the permission of American Physical Society from L. Zheng et. al. *Phys. Rev. Appl.* 9, 061002 (2018). [41])

The nanoscale resolution of TMIM also enables the observation of wave diffraction. LiNbO₃ wafers poled to be a single ferroelectric domain are energetically unstable. Over an

extended period, small domains with opposite polarization may spontaneously form to reduce the electrostatic energy. As discussed in the previous section, the domain inversion flips the sign of odd-rank tensors (polarization, 1st rank; piezoelectric tensor, 3rd rank), while leaving the even-rank tensors (permittivity, 2nd rank; elasticity tensor, 4th rank) unchanged [46]. Since the acoustic impedance mostly depends on the density and elasticity of the material, the SAW displacement field is not strongly affected by the domain structure. In contrast, the SAW electric field, which is the gradient of the SAW potential, changes sign across a domain wall due to the piezoelectric coupling. In this sample, a small domain with spontaneous polarization reversal is found near the left IDT (AFM image in Fig. 8a), as seen in the piezo-force microscopy (PFM) image in Fig. 8b. Since its dimension is comparable to the acoustic wavelength, wave diffraction is expected around the domain. In Fig. 8c, the TMIM surface potential map indeed displays very strong distortion of the wave front in this region. It is also important to note that the RMIM image (Fig. 8d) taken in the same region and at the same frequency only exhibits weak interference rings as discussed before, indicative of the different contrast mechanisms between the two modes of MIM.

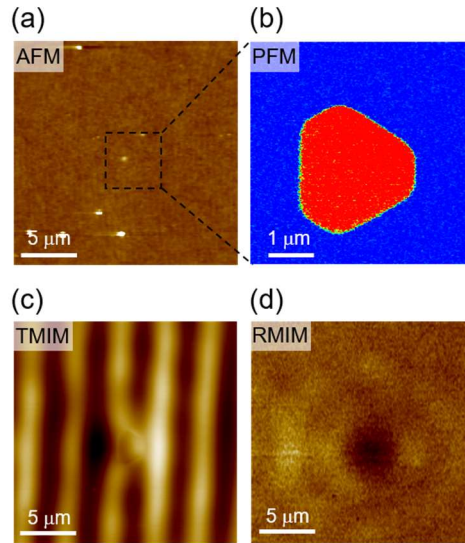


Figure 8. (a) AFM image in an area (blue dashed square in Fig. 6a) with a spontaneously reversed domain. (b) Close-up view of the PFM phase image inside the dashed square of (a). (c) TMIM and (d) RMIM images in the same area [41]. (*Printed with the permission of American Physical Society from L. Zheng et. al. Phys. Rev. Appl. 9, 061002 (2018). [41]*)

The capability to resolve the spatial distribution of SAW potential is of particular interest to integrated phononic systems. For instance, when designing SAW resonators [20, 59, 60], which feature stronger electrical coupling and better confinement than the micromechanical counterparts, it is desirable to directly compare the simulated and measured spatial distribution of energy

intensity of each acoustic cavity mode. In a recent report, a high-Q and small-mode-size SAW resonator on LiNbO_3 was demonstrated by engineering phononic band structures using adiabatically tapered structures [61]. As shown in Fig. 9a, the resonator consists of tapered couplers to enhance coupling to the source, phononic crystal sections to confine the phononic modes, and the resonant cavity. Compared to conventional Fabry-Perot resonators [20] that employ unperturbed free surfaces at the center and Bragg mirrors on the sides, the tapered grooves adiabatically change the reflectivity, resulting in a significantly reduced scattering loss of acoustic waves into the bulk and better confinement of phonons.

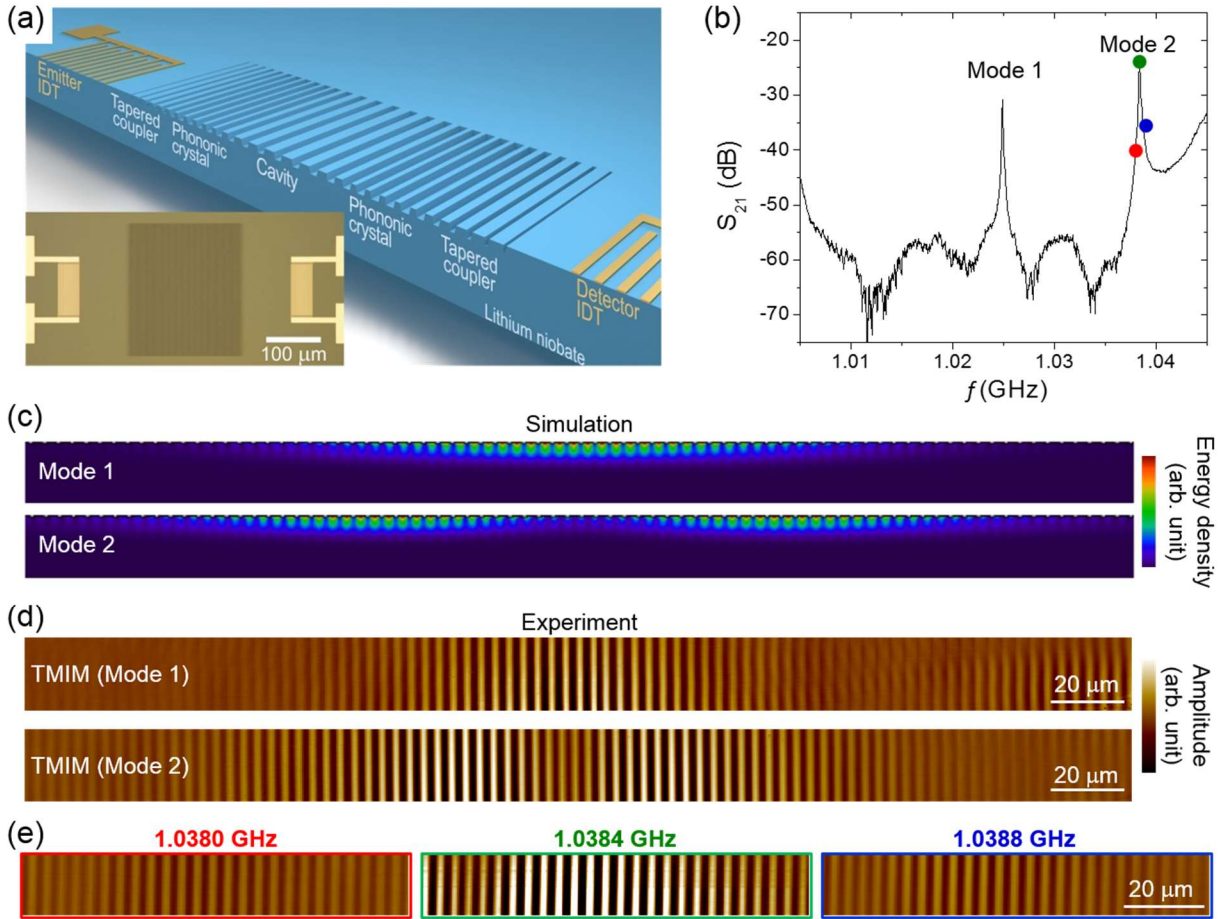


Figure 9. (a) Illustration of the SAW resonator on LiNbO_3 . The inset shows the optical microscope image of the fabricated device. The dark region at the center is the etched grooves, and the bright regions on the sides are metal IDTs. (b) Transmission spectrum of a SAW resonator, showing the two high-Q modes in the bandgap of the phononic crystal. Note that the data are slightly different from that in Ref. [61] due to the use of a different device. (c) Mode profiles of the fundamental and second-order modes of the SAW resonator. The color scale indicates the total energy density of electromagnetic, kinetic, and elastic energy densities. (d) TMIM images of the measured SAW potential distribution at both modes [61]. (e) TMIM images at three different frequencies. The scanned area is centered at the right antinode of Mode 2. Color coding of the borders here matches that of the dots in (b). (Printed with

the permission of American Physical Society from L. Shao et. al. Phys. Rev. Appl. 12, 014022 (2019). [61]

The SAW resonator device was designed to have two high-Q modes, which are indeed observed in the S_{21} spectra measured by a vector network analyzer (Fig. 9b). The period of the central cavity part is fine-tuned to align the resonant frequency of the fundamental mode to the center of phononic crystal bandgap. Fig. 9c displays the simulated energy density profiles of the fundamental (Mode 1) and second-order (Mode 2) modes of the SAW resonator. As shown in Fig. 9d, the single antinode in the middle of the resonator in Mode 1 and dual antinodes in Mode 2 are vividly seen in the SAW potential map measured by the TMIM [61]. The high quality of these modes can be further confirmed by taking TMIM data near the resonant frequency, as depicted in Fig. 9e. The substantial fall-off of the TMIM signal strength within 1 MHz around $f = 1.0384$ GHz is a direct evidence of the high-Q factor ($\sim 10,000$) of the second-order mode. We emphasize that, while the simulation and S_{21} measurement demonstrate the basic function, the spatially resolved TMIM images offer much more information on each section of the device. In-depth analysis of the local SAW images may reveal the effect of fabrication imperfections, crystal defects, and scattering from other phonons, which will provide insights on further improvement of the device performance.

Outlook

Compared with the widespread applications of near-field microwave microscopy in condensed matter physics, material science, device engineering, and biological research (covered by other topics in this special issue), the journey of microwave imaging on acoustic properties has just begun. In contrast to the synchrotron-based stroboscopic x-ray topography [16 – 18] and highly specialized scanning laser interferometry [21 – 23], the compatibility with tabletop AFM platforms makes the MIM a handy tool for individual laboratories. The nanoscale spatial resolution and the accessibility to high-GHz microwaves are also desirable for next-generation SAW devices with higher operation frequencies.

The reflection-mode MIM has now developed to an important scientific instrument for the study of local dielectric constant [62], dielectric loss [63], and electronic conductivity [64]. In piezoelectrics, the results reviewed here highlight a new contrast mechanism due to electromechanical energy transduction. When imaging multi-domain ferroelectric samples, it is

imperative to include the contribution of acoustic waves in the data interpretation. Conversely, careful analysis of the RMIM results on novel multiferroics may uncover the intimate coupling of electric and strain/stress fields in these systems. The study may open a research frontier to explore various nanoscale elastic phenomena in these systems by electromagnetic imaging.

The transmission-mode MIM is clearly advantageous for the imaging of SAW electric field in various devices such as delay lines, filters, and oscillators. While the demonstration above was performed in LiNbO₃, it is straightforward to expand the study to other popular acoustic materials such as quartz, AlN, GaAs, and ZnO. More importantly, SAWs at the frequency of 1 – 10 GHz have attracted great interest in quantum science and engineering as an efficient means to couple superconducting qubits [65 – 67], drive spin qubits [68 – 70], manipulate photons [71 – 73], and control two-dimensional (2D) electrons [74 – 76]. Direct visualization of the SAW potential in different platforms will help with the understanding of quantum entanglement, quantum hybrid networks, and deterministic teleportation of electrons. At the time of this writing, the authors are actively engaged along this line of research and a number of publications are forthcoming [77, 78].

Another potentially fruitful area for TMIM is 2D piezoelectric phononic crystals [13, 15], which are artificial structures formed through periodic spatial modulation of the elastic impedance. Through phonon-polariton coupling between electromagnetic waves and acoustic phonons, it is possible to form a complete band gap that phonons cannot propagate in all directions [15]. The spatial distribution of acoustic fields inside the 2D structures, which is only obtainable by numerical simulation at present, is crucial to advance this branch of research. Moreover, through band structure engineering, one may even realize topological phononic crystals with robust edge channels [79]. The topological protection against acoustic defects will be vividly demonstrated by TMIM imaging. Interestingly, a major research direction of the RMIM is to investigate the electronic topological edges in quantum Hall [80] and quantum spin Hall [81] systems, as reviewed by Rubin et al. in this issue. In that sense, MIM may be the technique of choice to visualize topological boundary states in both real materials and metamaterials.

In summary, the research of near-field microwave microscopy has expanded to the realm of acoustic waves in the past few years. It is now possible to probe acousto-electronic behaviors in SAW devices, quantum materials, and phononic crystals with nanoscale spatial resolution. With

continuous effort in this direction, we anticipate that exciting microwave microscopy works on acoustic waves will take place in the next few years.

References

- [1] C. Kittel, *Introduction to Solid State Physics*, 8th Edition, 2005 John Wiley & Sons, Inc.
- [2] H. E. Bommel and K. Dransfeld, “Excitation of very high frequency sound in quartz,” *Phys. Rev. Lett.* **1**, 234 (1958).
- [3] E. H. Jacobsen, “Piezoelectric Production of Microwave Phonons”, *Phys. Rev. Lett.* **2**, 249 (1959).
- [4] V. E. Bottom, “A history of the quartz crystal industry in the USA”, *Proc. 35th Frequency Control Symp. IEEE*. pp. 3 – 21 (1981).
- [5] R. M. White and F. W. Voltmer, “Direct piezoelectric coupling to surface elastic waves”, *Appl. Phys. Lett.* **7**, 314 (1965).
- [6] Lord Rayleigh, “On Waves Propagated along the Plane Surface of an Elastic Solid”, *Proc. London Math. Soc.* **s1-17**, 4 (1885).
- [7] K.-y. Hashimoto, *Surface Acoustic Wave Devices in Telecommunications – Modeling and Simulation*, Springer-Verlag, Berlin, 2000.
- [8] R. Weigel, D. P. Morgan, J. M. Owens, A. Ballato, K. M. Lakin, K.-y. Hashimoto, and C. C. W. Ruppel, “Microwave Acoustic Materials, Devices, and Applications”, *IEEE Trans. Microw. Theory Tech.* **50**, 738 (2002).
- [9] <https://www.everythingrf.com/News/details/8020-SAW-Device-Market-to-Grow-to-US-3-4-Billion-by-2024>
- [10] Y.-Q. Lu, Y.-Y. Zhu, Y.-F. Chen, S.-N. Zhu, N.-B. Ming, Y.-J. Feng, “Optical Properties of an Ionic-Type Phononic Crystal”, *Science* **284**, 1822 (1999).
- [11] Y.-y. Zhu, X.-j. Zhang, Y.-q. Lu, Y.-f. Chen, S.-n. Zhu, and N.-b. Ming, “New Type of Polariton in a Piezoelectric Superlattice”, *Phys. Rev. Lett.* **90**, 053903 (2003).
- [12] C.-p. Huang and Y.-y. Zhu, “Piezoelectric-Induced Polariton Coupling in a Superlattice”, *Phys. Rev. Lett.* **94**, 117401 (2005).
- [13] R.-C. Yin, C. He, M.-H. Lu, Y.-Q. Lu, and Y.-F. Chen, “Polaritons in an artificial ionic-type crystal made of two-dimensional periodically inverted multi-domain ferroelectric crystals”, *J. Appl. Phys.* **109**, 064110 (2011).

[14] D. Yudistira, A. Boes, D. Janner, V. Pruneri, J. Friend, and A. Mitchell, “Polariton-based band gap and generation of surface acoustic waves in acoustic superlattice lithium niobate”, *J. Appl. Phys.* **114**, 054904 (2013).

[15] D. Yudistira, A. Boes, B. Djafari-Rouhani, Y. Pennec, L. Y. Yeo, A. Mitchell, and J. R. Friend, “Monolithic Phononic Crystals with a Surface Acoustic Band Gap from Surface Phonon-Polariton Coupling”, *Phys. Rev. Lett.* **113**, 215503 (2014).

[16] R. W. Whatmore, P. A. Goddard, B. K. Tanner, and G. F. Clark, “Direct imaging of travelling Rayleigh waves by stroboscopic X-ray topography”, *Nature* **299**, 44 (1982).

[17] E. Zolotoyabko, D. Shilo, W. Sauer, E. Pernot and J. Baruchel, “Visualization of 10 μm surface acoustic waves by stroboscopic x-ray topography”, *Appl. Phys. Lett.* **73**, 2278 (1998).

[18] W. Sauer, M. Streibl, T. H. Metzger, A. G. C. Haubrich, S. Manus, A. Wixforth, J. Peisl, A. Mazuelas, J. Härtwig, and J. Baruchel, “X-ray imaging and diffraction from surface phonons on GaAs”, *Appl. Phys. Lett.* **75**, 1709 (1999).

[19] A. Mahjoubfar, K. Goda, A. Ayazi, A. Fard, S. H. Kim, and B. Jalali, “High-speed nanometer-resolved imaging vibrometer and velocimeter”, *Appl. Phys. Lett.* **98**, 101107 (2011).

[20] Y. Xu, W. Fu, C.-l. Zou, Z. Shen, and H. X. Tang, “High quality factor surface Fabry-Perot cavity of acoustic waves”, *Appl. Phys. Lett.* **112**, 073505 (2018).

[21] Y. Sugawara, O. B. Wright, O. Matsuda, M. Takigahira, Y. Tanaka, S. Tamura, and V. E. Gusev, “Watching Ripples on Crystals”, *Phys. Rev. Lett.* **88**, 185504 (2002).

[22] D. M. Profunser, O. B. Wright, and O. Matsuda, “Imaging Ripples on Phononic Crystals Reveals Acoustic Band Structure and Bloch Harmonics”, *Phys. Rev. Lett.* **97**, 055502 (2006).

[23] O. B. Wright and O. Matsuda, “Watching surface waves in phononic crystals”, *Phil. Trans. R. Soc. A* **373**, 20140364 (2015).

[24] D. V. Roshchupkin, Th. Fournier, M. Brunel, O. A. Plotitsyna, and N. G. Sorokin, “Scanning electron microscopy observation of excitation of the surface acoustic waves by the regular domain structures in the LiNbO₃ crystals”, *Appl. Phys. Lett.* **60**, 2330 (1992).

[25] D. V. Roshchupkin, M. Brunel, R. Tucoulou, E. Bigler, and N. G. Sorokin, “Reflection of surface acoustic waves on domain walls in a LiNbO₃ crystal”, *Appl. Phys. Lett.* **64**, 164 (1994).

[26] D. V. Roshchupkin and M. Brunel, “Scanning Electron Microscopy Observation of Surface Acoustic Wave Propagation in the LiNbO₃ Crystals with Regular Domain Structures”, *IEEE Trans. Ultrason. Ferroelectr. Freq. Control* **41**, 512 (1994).

[27] T. Hesjedal, and G. Behme, “High-resolution imaging of surface acoustic wave scattering”, *Appl. Phys. Lett.* **78**, 1948 (2001).

[28] T. Hesjedal and G. Behme, “AFM observation of surface acoustic waves emitted from single symmetric SAW transducers”, *IEEE Trans. Ultrason. Ferroelectr. Freq. Control Lett.* **48** 641 (2001).

[29] G. Behme and T. Hesjedal, “Influence of surface acoustic waves on lateral forces in scanning force microscopies”, *J. Appl. Phys.* **89**, 4850 (2001).

[30] T. Hesjedal and G. Behme, “High-resolution imaging of a single circular surface acoustic wave source: Effects of crystal anisotropy”, *Appl. Phys. Lett.* **79**, 1054 (2001).

[31] T. Hesjedal, “Surface acoustic wave-assisted scanning probe microscopy – a summary”, *Rep. Prog. Phys.* **73** 016102 (2010).

[32] I. Yahyaie, D. A. Buchanan, G. E. Bridges, D. J. Thomson, and D. R. Oliver, “High-Resolution Imaging of Gigahertz Polarization Response Arising From the Interference of Reflected Surface Acoustic Waves”, *IEEE Trans. Ultrason. Ferroelectr. Freq. Control* **59**, 121 (2012).

[33] K. Takata, T. Hasegawa, S. Hosaka, S. Hosoki, and T. Komoda, “Tunneling acoustic microscope”, *Appl. Phys. Lett.* **55**, 1718 (1989).

[34] W. Rohrbeck, E. Chilla, H.-J. Fröhlich, and J. Riedel, “Detection of surface acoustic waves by scanning tunneling microscopy”, *Appl. Phys. A* **52**, 344 (1991).

[35] E. Chilla, W. Rohrbeck, H.-J. Fröhlich, R. Koch, and K. H. Rieder, “Probing of surface acoustic wave fields by a novel scanning tunneling microscopy technique: Effects of topography”, *Appl. Phys. Lett.* **61**, 3107 (1992).

[36] T. Hesjedal, E. Chilla, and H.-J. Fröhlich, “Direct visualization of the oscillation of Au (111) surface atoms”, *Appl. Phys. Lett.* **69**, 354 (1996).

[37] B. A. Richardson, and G. S. Kino, “Probing of Elastic Surface Waves in Piezoelectric Media”, *Appl. Phys. Lett.* **16**, 82 (1970).

[38] Y. L. Yang, K. Lai, Q. Tang, W. Kundhikanjana, M. A Kelly, K. Zhang, Z.-X. Shen, and X. Li, “Batch-fabricated cantilever probes with electrical shielding for nanoscale dielectric and conductivity imaging”, *J. Micromech. Microeng.* **22**, 115040 (2012).

[39] K. Lai, W. Kundhikanjana, M. Kelly, and Z. X. Shen, “Modeling and characterization of a cantilever-based near-field scanning microwave impedance microscope”, *Rev. Sci. Instrum.* **79**, 063703 (2008).

[40] K. Lai, W. Kundhikanjana, M. Kelly, and Z. X. Shen, Nanoscale microwave microscopy using shielded cantilever probes”, *Appl. Nanosci.* **1**, 13 (2011).

[41] L. Zheng, D. Wu, X. Wu, and K. Lai, “Visualization of Surface-Acoustic-Wave Potential by Transmission-Mode Microwave Impedance Microscopy”, *Phys. Rev. Appl.* **9**, 061002 (2018).

[42] A. S. Thanawalla, S. K. Dutta, C. P. Vlahacos, D. E. Steinhauer, B. J. Feenstra, Steven M. Anlage, F. C. Wellstood, and R. B. Hammond, “Microwave near-field imaging of electric fields in a superconducting microstrip resonator”, *Appl. Phys. Lett.* **73**, 2491 (1998).

[43] S. K. Dutta, C. P. Vlahacos, D. E. Steinhauer, Ashfaq S. Thanawalla, B. J. Feenstra, F. C. Wellstood, S. M. Anlage, and H. S. Newman, “Imaging microwave electric fields using a near-field scanning microwave microscope”, *Appl. Phys. Lett.* **74**, 156 (1999).

[44] K. Lai, T. Ma, X. Bo, S. Anlage, and G. Shvets, “Experimental Realization of a Reflections-Free Compact Delay Line Based on a Photonic Topological Insulator”, *Sci. Rep.* **6**, 28453 (2016).

[45] F. Gao, H. Xue, Z. Yang, K. Lai, Y. Yu, X. Lin, Y. Chong, G. Shvets, and B. Zhang, “Topologically protected refraction of robust kink states in valley photonic crystals”, *Nature Phys.* **14**, 140 (2018).

[46] R. S. Weis and T. K. Gaylord, “Lithium Niobate: Summary of Physical Properties and Crystal Structure”, *Appl. Phys. A* **37**, 191 (1985).

[47] J. Slobodnik Jr., P. H. Carr, and A. J. Budreau, “Microwave Frequency Acoustic Surface-Wave Loss Mechanisms on LiNbO_3 ”, *J. Appl. Phys.* **41**, 4380 (1970).

[48] K. Yamanouchi and K. Shibayama, “Propagation and Amplification of Rayleigh Waves and Piezoelectric Leaky Surface Waves in LiNbO_3 ”, *J. Appl. Phys.* **43**, 856 (1972).

[49] M. Yamada, N. Nada, M. Saitoh, and K. Watanabe, “First-order quasi-phase matched LiNbO_3 waveguide periodically poled by applying an external field for efficient blue second-harmonic generation”, *Appl. Phys. Lett.* **62**, 435 (1993).

[50] H. Liang, R. Luo, Y. He, H. Jiang, and Q. Lin, “High-quality lithium niobate photonic crystal nanocavities”, *Optica* **4**, 1251 (2017).

[51] L. Zheng, H. Dong, X. Wu, Y.-L. Huang, W. Wang, W. Wu, Z. Wang, and K. Lai, “Interferometric imaging of nonlocal electromechanical power transduction in ferroelectric domains”, *Proc. Natl. Acad. Sci.* **115**, 5338 (2018).

[52] S. R. Johnston, Y. Yang, Y.-T. Cui, E. Y. Ma, T. Kämpfe, L. M. Eng, J. Zhou, Y.-F. Chen, M. Lu, and Z.-X. Shen, “Measurement of surface acoustic wave resonances in ferroelectric domains by microwave microscopy”, *J. Appl. Phys.* **122**, 074101 (2017).

[53] A. Takayanagi, K. Yamanouchi, and K. Shibayama, “Piezoelectric leaky surface wave in LiNbO_3 ”, *Appl. Phys. Lett.* **17**, 225 (1970).

[54] D. Royer and E. Dieulesaint, *Elastic Waves in Solids*, Springer-Verlag 1999.

[55] J. L. Bleustein, “A New Surface Wave in piezoelectric materials”, *Appl. Phys. Lett.* **13**, 412 (1968).

[56] Y. V. Gulyaev, “Electroacoustic surface waves in piezoelectric materials”, *JETP Lett.* **9**, 37 (1969).

[57] R. M. White, “Surface Elastic Waves”, *Proc. IEEE* **58**, 1238 (1970).

[58] M. F. Crommie, C. P. Lutz, and D. M. Eigler, “Confinement of Electrons to Quantum Corrals on a Metal Surface”, *Science* **262**, 218 (1993).

[59] S. Fujii, T. Odawara, H. Yamada, T. Omori, K. Hashimoto, H. Torii, H. Umezawa, and S. Shikata, “Low propagation loss in a one-port SAW resonator fabricated on single-crystal diamond for super-high-frequency applications”, *IEEE Trans. Ultrason. Ferroelectr. Freq. Control* **60**, 986 (2013).

[60] R. Manenti, M. J. Peterer, A. Nersisyan, E. B. Magnusson, A. Patterson, and P. J. Leek, “Surface acoustic wave resonators in the quantum regime”, *Phys. Rev. B* **93**, 041411(R) (2016).

[61] L. Shao, S. Maity, L. Zheng, L. Wu, A. Shams-Ansari, Y.-I. Sohn, E. Puma, M. N. Gadalla, M. Zhang, C. Wang, K. Lai, and M. Loncar, “Phononic Band Structure Engineering for High-Q Gigahertz Surface Acoustic Wave Resonators on Lithium Niobate”, *Phys. Rev. Appl.* **12**, 014022 (2019).

[62] D. Wu, A. J Pak, Y. Liu, Y. Zhou, X. Wu, Y. Zhu, M. Lin, Y. Han, Y. Ren, H. Peng, Y.-H. Tsai, G. S. Hwang, K. Lai, “Thickness-Dependent Dielectric Constant of Few-Layer In_2Se_3 Nanoflakes”, *Nano Lett.* **15**, 8136 (2015).

[63] X. Wu, U. Petralanda, L. Zheng, Y. Ren, R. Hu, S.-W. Cheong, S. Artyukhin, K. Lai, “Low-energy Structural Dynamics of Ferroelectric Domain Walls in Hexagonal Rare-earth Manganites”, *Sci. Adv.* **3**, e1602371 (2017).

[64] D. Wu, X. Li, L. Luan, X. Wu, W. Li, M. N. Yogeesh, R. Ghosh, Z. Chu, D. Akinwande, Q. Niu, and K. Lai, “Uncovering edge states and electrical inhomogeneity in MoS₂ field-effect transistors”, *Proc. Natl. Acad. Sci.* **113**, 8583 (2016).

[65] Y. Chu, P. Kharel, W. H. Renninger, L. D. Burkhardt, L. Frunzio, P. T. Rakich, and R. J. Schoelkopf, “Quantum acoustics with superconducting qubits”, *Science* **358**, 199 (2017).

[66] M. Kervinen, I. Rissanen, and M. Sillanpää, “Interfacing planar superconducting qubits with high overtone bulk acoustic phonons”, *Phys. Rev. B* **97**, 205443 (2018).

[67] P. Arrangoiz-Arriola, E. A. Wollack, M. Pechal, J. D. Witmer, J. T. Hill, and A. H. Safavi-Naeini, “Coupling a Superconducting Quantum Circuit to a Phononic Crystal Defect Cavity”, *Phys. Rev. X* **8**, 031007 (2018).

[68] M. J. A. Schuetz, E. M. Kessler, G. Giedke, L. M. K. Vandersypen, M. D. Lukin, and J. I. Cirac, “Universal Quantum Transducers Based on Surface Acoustic Waves”, *Phys. Rev. X* **5**, 031031 (2015).

[69] D. A. Golter, T. Oo, M. Amezcuia, K. A. Stewart, and H. Wang, “Optomechanical Quantum Control of a Nitrogen-Vacancy Center in Diamond”, *Phys. Rev. Lett.* **116**, 143602 (2016).

[70] S. J. Whiteley, G. Wolfowicz, C. P. Anderson, A. Bourassa, H. Ma, M. Ye, G. Koolstra, K. J. Satzinger, M. V. Holt, F. J. Heremans, A. N. Cleland, D. I. Schuster, G. Galli, and D. D. Awschalom, “Spin–phonon interactions in silicon carbide addressed by Gaussian acoustics”, *Nat. Phys.* **15**, 490 (2019).

[71] S. A. Tadesse and M. Li, “Sub-optical wavelength acoustic wave modulation of integrated photonic resonators at microwave frequencies”, *Nat. Commun.* **5**, 5402 (2014).

[72] S. Kapfinger, T. Reichert, S. Lichtmannecker, K. Muller, J. J. Finley, A. Wixforth, M. Kaniber, and H. J. Krenner, “Dynamic acousto-optic control of a strongly coupled photonic molecule”, *Nat. Commun.* **6**, 8540 (2015).

[73] K. Fang, M. H. Matheny, X. Luan, and O. Painter, “Optical transduction and routing of microwave phonons in cavity-optomechanical circuits”, *Nat. Photon.* **10**, 489 (2016).

[74] S. Hermelin, S. Takada, M. Yamamoto, S. Tarucha, A. D. Wieck, L. Saminadayar, C. Bauerle, and T. Meunier, “Electrons surfing on a sound wave as a platform for quantum optics with flying electrons”, *Nature* **477**, 435 (2011).

[75] R. P. G. McNeil, M. Kataoka, C. J. B. Ford, C. H. W. Barnes, D. Anderson, G. A. C. Jones, I. Farrer, and D. A. Ritchie, “On-demand single-electron transfer between distant quantum dots”, *Nature* **477**, 439 (2011).

[76] M. J. A. Schuetz, J. Knörzer, G. Giedke, L. M. K. Vandersypen, M. D. Lukin, and J. I. Cirac, “Acoustic Traps and Lattices for Electrons in Semiconductors”, *Phys. Rev. X* **7**, 041019 (2017).

[77] L. Shao, M. Yu, S. Maity, N. Sinclair, L. Zheng, C. Chia, A. Shams-Ansari, C. Wang, M. Zhang, K. Lai, and M. Lončar, “Microwave-to-optical conversion using lithium niobate thin-film acoustic resonators”, *Optica* **6**, 1498 (2019).

[78] S. Maity, L. Shao, S. Bogdanović, S. Meesala, Y.-I. Sohn, N. Sinclair, B. Pingault, M. Chalupnik, C. Chia, L. Zheng, K. Lai, and M. Lončar, “Coherent acoustic control of a single silicon vacancy spin in diamond”, *Nature Commun.* **11**, 193 (2020).

[79] P. Wang, L. Lu, and K. Bertoldi, “Topological Phononic Crystals with One-Way Elastic Edge Waves”, *Phys. Rev. Lett.* **115**, 104302 (2015).

[80] K. Lai, W. Kundhikanjana, J. Shabani, M. Shayegan, M.A. Kelly, and Z.-X. Shen, “Imaging of the Coulomb driven quantum Hall edge states”, *Phys. Rev. Lett.* **107**, 176809 (2011).

[81] E. Y. Ma, M. R. Calvo, J. Wang, B. Lian, M. Muhlbauer, C. Brune, Y.-T. Cui, K. Lai, W. Kundhikanjana, Y. Yang, M. Baenninger, M. Konig, C. Ames, H. Buhmann, P. Leubner, L. W. Molenkamp, S.-C. Zhang, D. Goldhaber-Gordon, M. A. Kelly, Z.-X. Shen, “Unexpected edge conduction in mercury telluride quantum wells under broken time-reversal symmetry”, *Nat. Commun.* **6**, 7252 (2015).

Side bar information (Page 1)

It should be noted that the term ‘elastic waves’ is often used when the emphasis is on the classical description of solids as continuous elastic media. The term ‘acoustic waves’, on the other hand, emphasizes the linear dispersion relation in the long-wavelength limit. In this article, we will continue to use ‘acoustic waves’ for a natural connection to other rapidly evolving fields such as acousto-electronics and acousto-optics.